

Modeling Geometrical Spreading and the Relative Amplitudes of Vertical and Horizontal High-Frequency Ground Motions in Eastern North America

by M. C. Chapman and R. W. Godbee

2 **Abstract** Horizontally layered velocity models were used with point-source and finite-fault sources to investigate geometrical spreading and the relative amplitudes of vertical and horizontal ground acceleration within 120 km of the source. Full wave-field simulations were done for a range of focal depths and for strike-slip and reverse focal mechanisms. The attenuation of the geometric mean of randomly oriented horizontal-component maximum acceleration amplitudes, averaged over all azimuths, significantly exceeds the theoretical geometrical spreading for far-field body waves in a homogeneous whole space for hypocentral distances less than approximately 60 km. The behavior of the vertical component is different from the horizontal: vertical attenuation near the epicenter is greater and is more dependent on source mechanism and depth. Because of the rapid near-source decay of the direct *S* wave, reflections from the mid-lower crust and Moho control the maximum amplitude of the vertical-component acceleration in the 60–120-km hypocenter distance range, resulting in a flattening of the vertical amplitude-distance relation. Near-source vertical maximum amplitudes averaged over all source–receiver azimuths tend to be less than the geometric mean horizontal amplitude for strike-slip focal mechanisms, but, near the source for reverse faults, the azimuthally averaged vertical-component amplitude exceeds that of the geometric mean horizontal. The modeling indicates that similar vertical- and horizontal-component geometrical spreading and approximately constant horizontal/vertical amplitude ratios observed in connection with the *Lg* phase at distances greater than approximately 100 km in eastern North America may not hold at smaller distances. Ground-motion prediction models for the vertical component near the source may need to incorporate strong geometrical spreading and dependence on radiation pattern.

Introduction

The amplitude of seismic waves radiated from an isotropic point source in a homogeneous elastic whole space, at source–receiver distance r , is inversely proportional to r in the far field. However, the velocity structure of the Earth is not homogenous, the earthquake radiation pattern is not isotropic, the source is finite in spatial extent, and the seismic wave field is usually experienced on an irregular free surface. Consequently, the amplitude–distance relation is complicated. It depends on details of the 3D velocity structure, the source radiation pattern, and depth. It also depends on frequency, due to the nature of the earthquake source spectrum, and to wave propagation effects involving anelastic loss and scattering. Details of the rupture process in both time and space strongly affect the wave field near the source of a large earthquake. Because of these and other complications, high-frequency ground motions near the source of large shocks are difficult

to model theoretically and empirical ground-motion prediction models developed from data recorded in seismically active areas remain the mainstay of earthquake engineering.

Lack of data makes empirical development of strong ground motion prediction models difficult in eastern North America. The data consist largely of recordings obtained at distances in excess of 100 km from earthquakes with magnitudes less than 6. Prior to the recent appearance of the EarthScope transportable array, few earthquakes had been recorded in the eastern United States with more than a handful of calibrated three-component stations at distances less than 100 km. The passage of the EarthScope transportable array through the region in the next few years will result in additional data in this important near-source distance range. **3**

We refer below to apparent geometrical spreading, $G(r)$, representing the frequency-independent loss of seismic-wave

amplitude with increasing hypocenter–receiver distance, r . Idealized far-field body-wave spreading in a homogeneous whole space is given by $G = r^{-1}$, and $G = r^{-0.5}$ represents idealized surface-wave spreading for a half-space. Theoretical studies indicate that apparent geometrical spreading in velocity structures other than a homogeneous whole space will generally involve other variables in addition to r . For example, [Ou and Herrmann \(1990\)](#) found that $G(r)$ may depend upon source depth in layered structures. [Burger *et al.* \(1987\)](#) note the importance of post-critical reflections from mid-lower crustal velocity discontinuities and the Moho in controlling amplitudes in certain distance ranges.

Empirical studies using data primarily from earthquakes in southeastern Canada and the northeastern United States report relatively rapid decay of ground-motion amplitude with distance for r less than approximately 60 km, with less rapid decay at distances exceeding approximately 120 km, and a zone of no attenuation (or increasing amplitude with distance) in the intervening distance range ([Atkinson and Mereu, 1992](#); [Atkinson, 2004](#)). The flattening of apparent attenuation and/or increase in amplitude observed from approximately 60 to 120 km has been attributed to large amplitude post-critical reflections from the mid-lower crust and Moho ([Burger *et al.*, 1987](#); [Atkinson, 2004](#)). The Lg phase begins to develop at approximately 120 km or somewhat beyond, depending on crustal structure. Lg is a crust-guided phase involving the reflection and interference of multipath shear waves interacting with the free surface and laterally extensive velocity contrasts in the crust and from the Moho. Lg travels with a group velocity of approximately 3.5 km/s and is the largest amplitude phase on all three components for a source in continental crust at distances exceeding approximately 120 km. It can be treated as the superposition of higher-mode surface waves, exhibiting geometrical spreading approximately as $r^{-0.5}$ ([Wang and Herrmann, 1980](#); [Herrmann and Kijko, 1983](#); [Kennett, 1986](#)).

The lack of well-recorded earthquakes in the distance range $r < 100$ km in eastern North America has prevented detailed empirical investigation of $G(r)$ in terms of other variables. Data from earthquakes in different crustal structure and with different focal depths and mechanisms, as well as recordings of vertical and horizontal components, have been combined to develop empirical prediction models in that distance range. The resulting scatter exhibited by the combination of these diverse data may be due to the effects of other variables in addition to r .

A related issue is the amplitude of the vertical component, relative to the horizontal components, near the source in eastern North America. Shallow crustal velocities in the mid-continent and Appalachian region are relatively high compared to those found in tectonically active areas, such as near major faults in California. Strong velocity contrasts exist in areas of eastern North America where Proterozoic to early-Mesozoic high-velocity volcanic, sedimentary, or crystalline rocks are overlain at shallow depth by alluvium or deposits of poorly consolidated Cretaceous and Cenozoic sediments,

such as in the Atlantic and Gulf coastal plains and the Mississippi embayment. Also, reverse faulting is common in parts of eastern North America, whereas the California strong-motion data set is dominated by strike-slip events (see [Data and Resources](#) section). The relationship between vertical and horizontal-component motions near the source in eastern North America may be different from that inferred from western U.S. data.

This study does not examine the behavior of Lg , but instead focuses on hypocenter distances less than 120 km where ground motions are the strongest and maximum acceleration amplitudes for rock sites are largely associated with body-wave phase arrivals. The objective is to characterize the theoretical behavior of $G(r)$, for horizontal and vertical components, due to strike-slip and reverse-faulting focal mechanisms for a range of focal depths. The modeling involves full-wave-field ground-motion simulations from both point-source and finite-fault models. The 1D velocity models used are representative of those typical of rock conditions in the midcontinent, the Appalachian region, the Atlantic coastal plain, and the Mississippi embayment.

Modeling Approach

Wave propagation effects were modeled using the frequency–wavenumber integration method. The computations were done using the program *hspec96*, version 3.3 ([Data and Resources](#) section). The program computes elemental Green’s functions that can be combined to create three-component time series for arbitrarily oriented point sources, double couples, and general moment tensors. The Green’s functions include all direct and scattered body waves and surface waves for a horizontally layered Earth model with anelastic attenuation. The computed wave field includes near-field and far-field components. The original source code was modified by the authors to include frequency-dependent Q .

The laterally isotropic 1D layered model we use is only an approximation to the real Earth. The 3D complexity of the Earth results in more multipathing, mostly composed of back-scattered waves (i.e., multiple reflections from points outside the plane of the source and receiver), than our 1D model produces. This 3D multipath backscattering is what generates much of the seismic coda, which is more intense as frequency increases. As a result, our acceleration simulations lack the duration of envelope motion that real accelerograms exhibit, yet the maximum acceleration amplitudes at high frequency seem to be realistic. Because the dominant frequencies are lower, our synthetic velocity waveforms look very much like real seismograms.

The seismic source was modeled using the [Zeng *et al.* \(1994\)](#) kinematic approach with minor modification. The source is comprised of a composite set of overlapping circular subfaults. The subfault radii are randomly distributed according to a power law with fractal dimension $D = 2$ ([Frankel, 1991](#)). We simulated an M 6.0 rupture of a square fault with length and width 6.49 km. The dimensions were

chosen to be consistent with the M 6.0 rupture of a circular fault with static stress drop of 10 MPa. The constant stress drop of the subfaults in the composite model is essentially a free parameter. It largely controls the high-frequency level of the source spectrum. It was constrained by adopting the high-frequency level of the Brune (1970) model (M 6.0, static stress drop 10 MPa) as a target for the simulation. The average amplitude of the high-frequency (> 10 Hz) level of the simulation source (moment-rate) spectrum matches that of the target using a subfault stress drop of 3.5 MPa. The simulation assumes a rupture velocity of 2.8 km/s, with rupture initiating at the center of the rupture zone (which, with the aspect ratio of a square fault, minimizes directivity effects and other source complexity).

Details of the source modeling and the calculations combining the source functions and Green's functions are contained in the Appendix. Green's functions were not computed for each subfault: the number of required Green's functions was reduced by gridding the fault area into 0.25×0.25 km² elements, summing the subfault source functions within a given grid element, and computing Green's functions for the grid elements rather than for all subfaults.

The main objective of the study was to characterize the nature of $G(r)$. The hypocentral distance range of primary interest is from $1.5h$ to 120 km, where h is focal depth. The minimum focal depth of the simulations is 7.25 km. Extensive comparisons of results derived using the point-source and finite-fault source for the M 6.0 earthquake modeled here indicate negligible differences in apparent geometric spreading in the distance range of interest, so many of the results presented below are based on point-source simulations. As described in the Appendix, the point-source model is simply the composite finite-fault source time function applied at a point, the hypocenter.

Velocity Models

Three velocity models were examined (Fig. 1). The rock-1 and rock-2 models were based on a review of crustal velocity models developed from long-range seismic refraction experiments in eastern North America (Braile, 1989; Braile *et al.*, 1989; Taylor, 1989; Chulick and Mooney, 2002). The models reflect the range of structures reported for the Appalachian region and adjacent parts of the craton in southeastern Canada. The crustal thickness of the rock-1 model is 36 km, and the velocity–depth profile is a stepwise increase in velocity approximating a linear gradient. The rock-2 crustal thickness is 40 km and features a sharp midcrustal velocity discontinuity with a high-velocity lower crust. The sediment model represents the structure in the Atlantic coastal plain in the vicinity of Charleston, South Carolina. The upper 0.75 km of the sediment model was derived from a sonic log and suspension logs described by Chapman *et al.* (2006). Detailed P - and S -wave velocities at shallow depths for the rock models are lacking. The uppermost 1 km of both rock models were based on reported S -wave velocities of approximately 2.6–3.0 km/s near the surface from a number of shallow geotechnical results in the eastern United States and the results of Beresnev and Atkinson (1997) for southeastern Canada. The shallow (0–0.75 km depth) P - and S -wave velocities for the rock-1 and rock-2 models were developed by assuming that Poisson's ratio is 0.25 and adjusting the sediment model S -wave velocity profile such as to produce 3.0 km/s velocity at the surface. Adopting this profile for the upper 0.75 km of the rock-1 and rock-2 models was judgmental: the objective was to model, at least to some degree, the decrease in velocity due to effects of near-surface open cracks and weathering. The effect of this modeled complexity at shallow depths in the rock models is mainly to introduce a small amplification

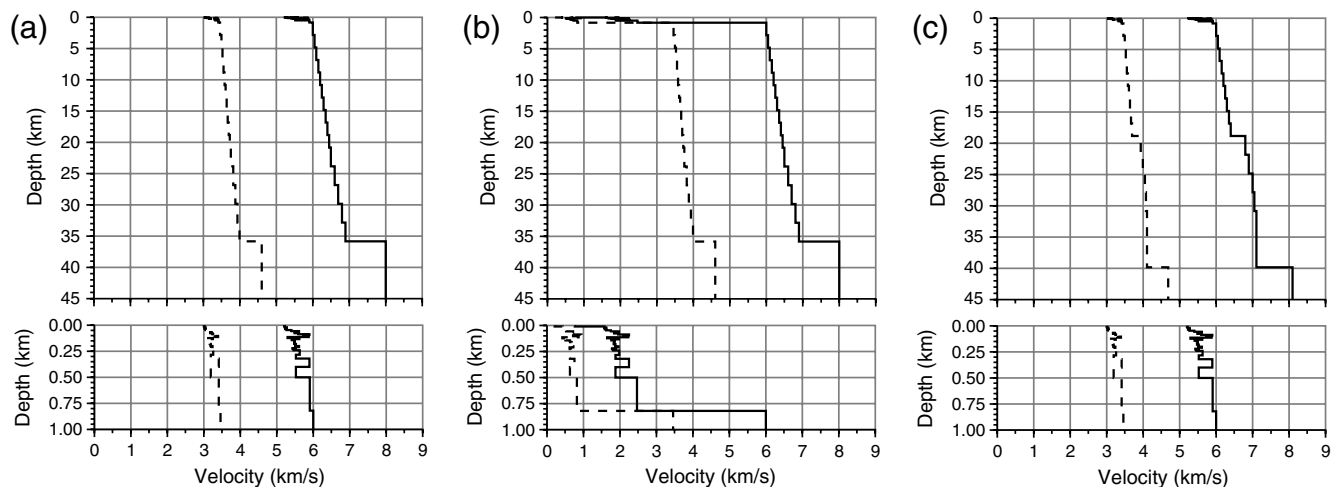


Figure 1. (a) Rock-1 velocity model. (b) Sediment model. (c) Rock-2 model. The dashed line shows S -wave velocities. The solid line shows P -wave velocities.

(and increased scattering effects) into the simulations, which creates a more realistic coda. Minor variation of the velocities and thicknesses of these shallow layers in the rock models have negligible effect on the apparent geometrical spreading. Anelastic attenuation for both rock models and the subsediment (deeper than 0.75 km) part of the sediment model was modeled using $Q(f) = 811f^{0.42}$ (Chapman and Rogers, 1989) for both P and S waves. A frequency-independent Q of 80 was used for P and S waves in all layers at depths less than 0.75 km in the sediment model (Chapman *et al.*, 2008).

Source–Receiver Locations

Figure 2 shows the two receiver patterns used. The finite-fault simulations were done using a square Cartesian grid of stations with receiver spacing of 1 km near the source, 2 km at intermediate distances (receiver x and y coordinates between ± 30 km and ± 60 km), and 4 km at larger distances. The point-source simulations were constructed for a pattern of receiver locations arranged as the spokes of a wheel with 5° separation; the radial receiver separation was 1 km.

Two focal mechanisms were modeled: right-lateral strike-slip on a vertical fault and reverse motion on a fault dipping 45° . The point of rupture initiation (hypocenter) for the finite fault and the point source was modeled at depths of 7.25, 12.25, 17.25, and 22.25 km.

Results

The simulated three-component ground accelerations were filtered using causal, four-pole Butterworth band-pass filters in the following frequency bands: 0.5–1.0, 1.0–2.0,

2.0–4.0, 4.0–8.0, 8.0–16.0, and 16.0–32.0 Hz. The strike-normal and strike-parallel horizontal components were reoriented by choosing a random, uniformly distributed rotation angle in the range 0° – 360° for each receiver. The geometric mean of the two maximum (absolute value) horizontal amplitudes was then calculated for each filter passband; that quantity is referred to below by the acronym “gmran.”

Figure 3 shows an example of the finite-fault simulation results in map view for a focal depth of 12.25 km and for both strike-slip and reverse mechanisms. The rock-1 velocity model was used for this example. The contours show maximum acceleration values in the 4–8 Hz passband. Figure 4 plots acceleration versus nearest fault-rupture distance for the finite-fault simulation example shown in Figure 3. The dispersion of the simulated maximum acceleration values at a given nearest fault-rupture distance is largest for the vertical component in the strike-slip simulation. This is largely an effect of the radiation pattern; and, interestingly, the dispersion of the vertical component in the reverse-fault simulation is less than for the geometric mean of the horizontal components for either of the two focal mechanisms. Figure 4 shows a difference in apparent geometrical spreading of the vertical component compared to the horizontal and a substantial difference between the vertical-component amplitudes for the two focal mechanisms. We further examine this behavior and its dependence on frequency, focal depth, and velocity structure in the following.

Figures 5 and 6 plot the unfiltered acceleration time series for the vertical and strike-normal horizontal components along a profile trending 22° from the strike direction of the finite-fault source (X direction in Figs. 2 and 3). Figure 5 shows results for the strike-slip fault simulation, and Figure 6

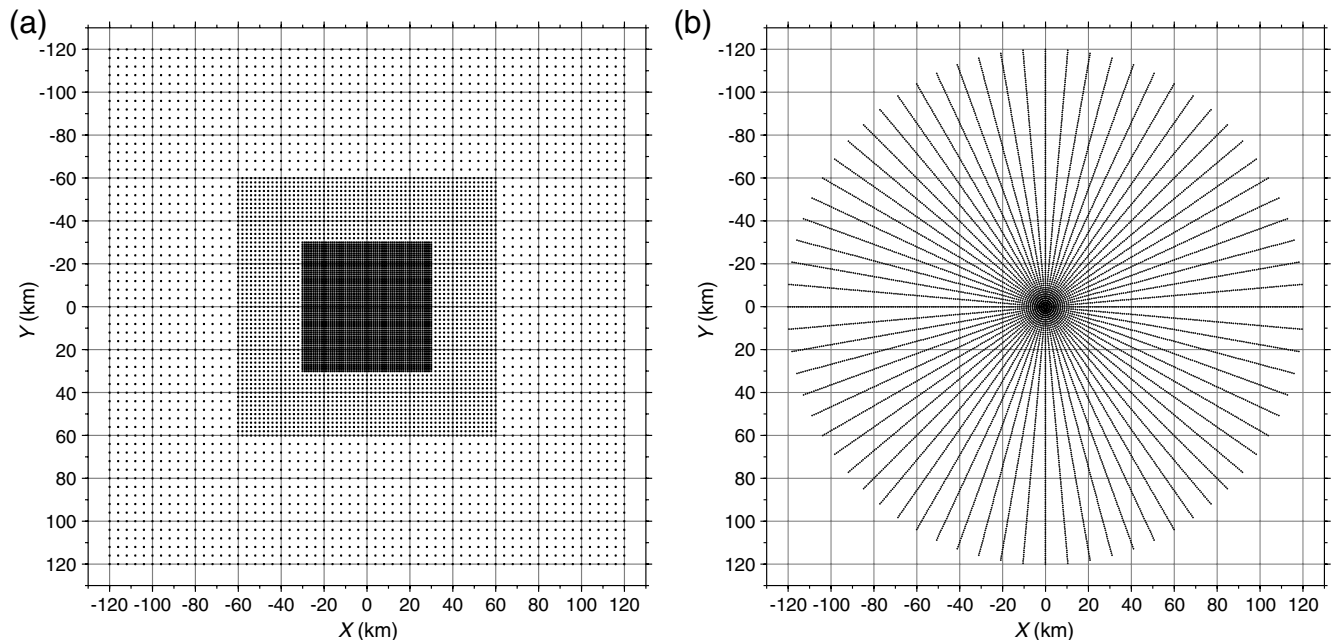


Figure 2. (a) Cartesian grid used for finite-fault simulation. (b) Polar grid used for point-source simulation.

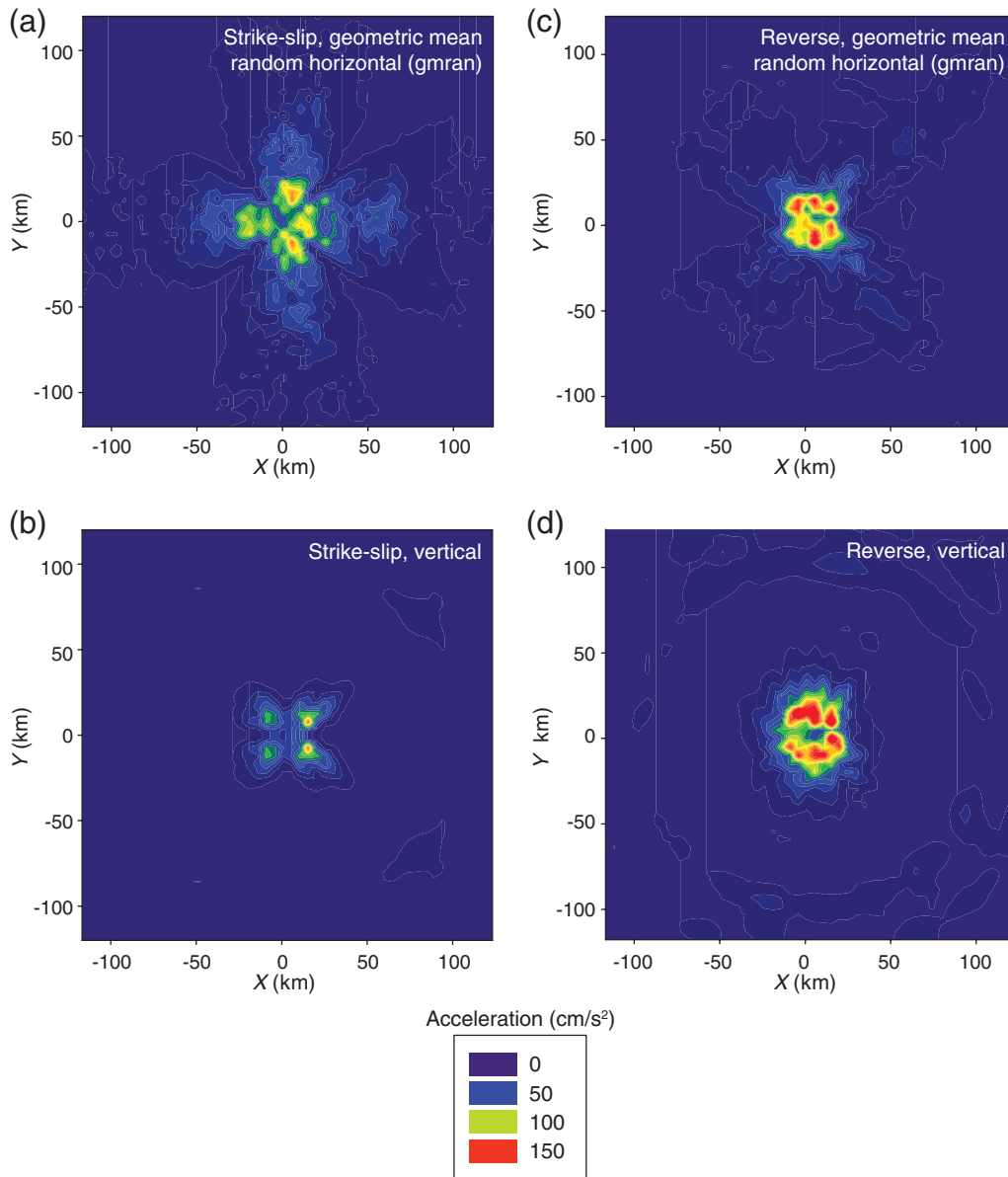


Figure 3. Simulated maximum acceleration amplitudes in the 4–8 Hz band for an $M 6.0$ event with center of rupture at 12.25 km depth, striking in the X direction. The rock-1 velocity model was used for the finite-fault simulation. (a,b) Geometric mean of the maximum amplitudes of two orthogonal randomly oriented horizontal components and the vertical component, respectively, for a right-lateral strike-slip focal mechanism. (c,d) Geometric mean of the maximum amplitudes of two orthogonal randomly oriented horizontal components and the vertical component, respectively, for a reverse-faulting mechanism, with the fault dipping 45° in the negative Y direction. The rupture initiation was at the center of a square rupture area, as described in the text.

shows results for the reverse-fault simulation. Rapid attenuation of the direct S wave on the vertical component in the hypocenter distance range of 20–60 km, compared to the strike-normal component, is apparent by comparing amplitudes that have been multiplied by the hypocenter distance r in order to correct for idealized $G(r)$. The direct S-wave amplitudes of the horizontal strike-normal component for both mechanisms decay with distance somewhat faster than r^{-1} , whereas the vertical component decays much faster. In the distance range of 80–120 km, the amplitude of the direct S wave on the vertical component is less than that of the SmS

reflection from the Moho (shown by arrows in Figs. 5 and 6). On the other hand, the direct S amplitude on the strike-normal horizontal component exceeds the Moho reflection amplitude in this distance range, although the amplitudes are similar, and both phases begin to merge at approximately 120 km.

Figure 7 again shows results in the 4–8 Hz passband, comparing results for the rock-1 and sediment velocity models using a point-source simulation. Plotted are the arithmetic mean values of maximum acceleration on the vertical and gmrn horizontal components, in 2 km-wide distance bins, as a function of hypocenter distance. The lines in Figure 7 are

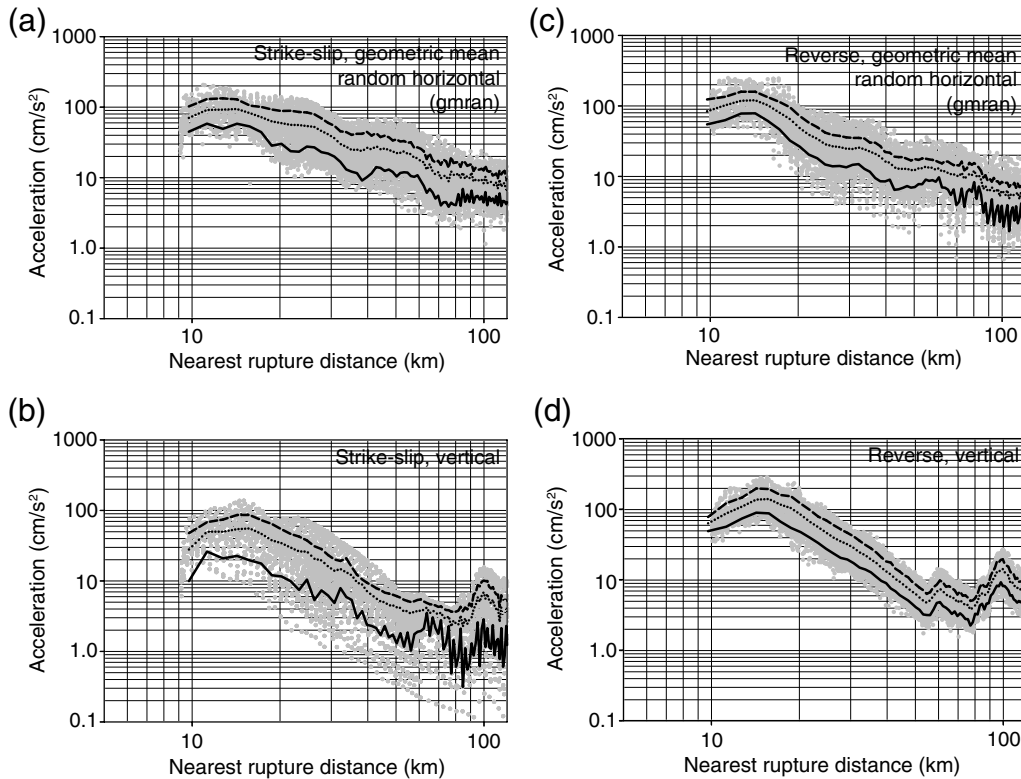


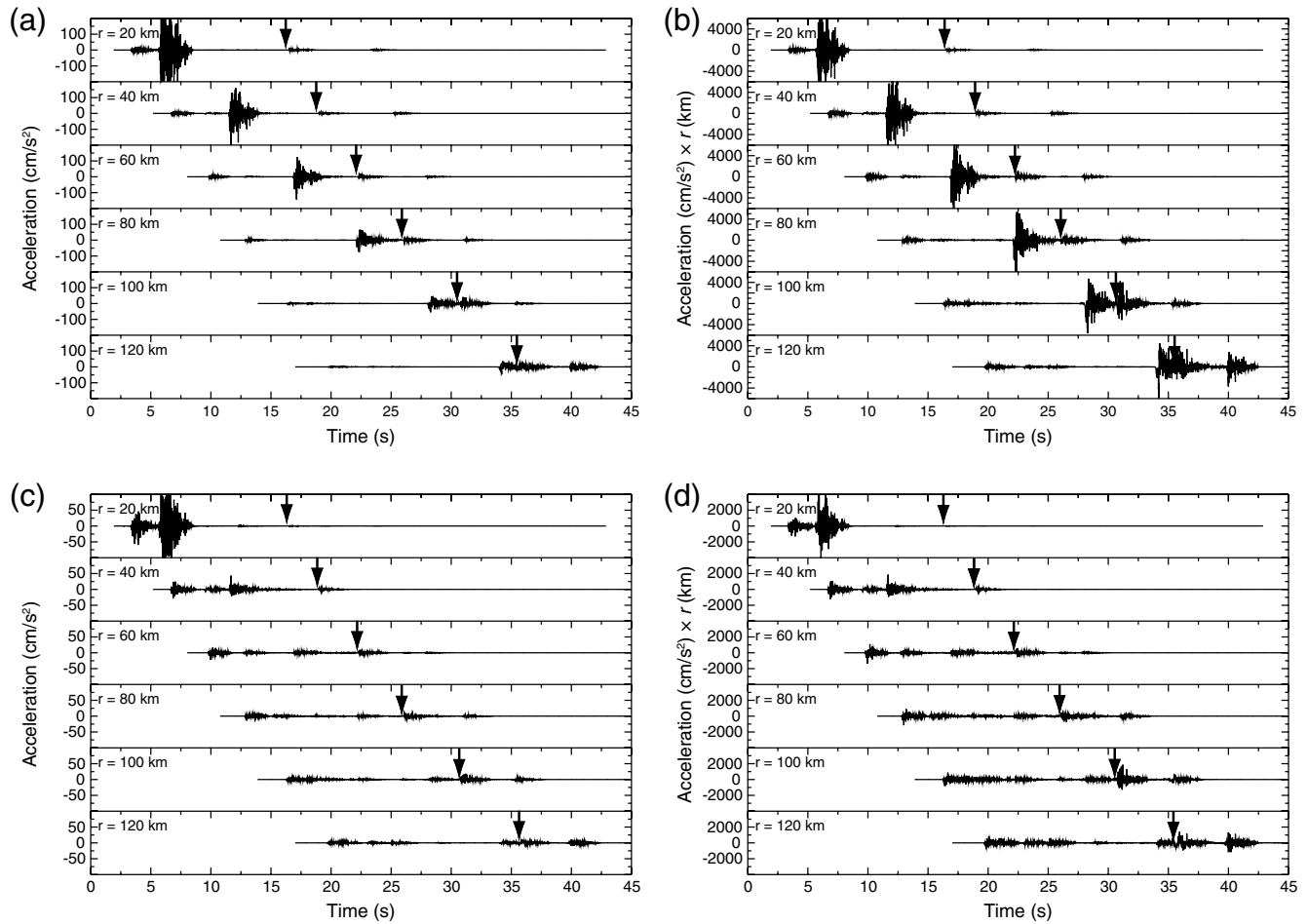
Figure 4. The grey dots show simulated maximum acceleration amplitudes in the 4–8 Hz band relative to distance to the nearest point of fault rupture, for an M 6.0 event with center of rupture (hypo-center) at 12.25 km depth, as shown in the map view in Figure 3. The rock-1 velocity model was used for the finite-fault simulation. (a,b) The geometric mean of the two randomly oriented orthogonal horizontal components and the vertical component, respectively, for a strike-slip focal mechanism. (c,d) The geometric mean of the two randomly oriented orthogonal horizontal components and the vertical component, respectively, for the reverse-faulting mechanism, with the fault dipping 45° . The arithmetic means of the simulated values in distance bins that are 2 km wide are shown by the short-dashed line: 16th and 84th percentile values are shown by the solid and long-dashed lines, respectively.

analogous to the short-dashed lines in Figure 4. Results for different focal depths are shown for both the reverse and strike-slip mechanisms. The sediment model amplifies the 4–8-Hz ground motion relative to the rock-1 model by a factor of approximately 2.5. Figure 7 also shows that the vertical-component peak motions exhibit different apparent geometrical spreading compared to the gmrh horizontal components. Outside the immediate epicentral area, the apparent attenuation of the vertical component as a function of hypocenter distance exhibits a steeper slope than that of the gmrh horizontal components. However, between 60 and 120 km, the amplitude–distance plot for the vertical component flattens, and the vertical amplitudes increase at certain distances in this 60–120-km range.

The mean gmrh horizontal-component amplitudes for the strike-slip mechanism appear to decay consistently throughout the distance range examined here, at a rate somewhat greater than r^{-1} for all focal depths examined and for both the rock-1 and sediment models. The horizontal-component amplitudes for the reverse mechanism and the rock-1 model are peaked in the epicentral area for focal depths of 12 and 22 km and then decay abruptly, thereafter following a trend similar to that exhibited for the strike-slip

mechanism. We note that vertical-component amplitudes, relative to the gmrh horizontal amplitudes, are larger for the reverse focal mechanism compared to the strike-slip mechanism, for both rock and sediment models. In the case of the rock model, the larger vertical-component amplitudes for the reverse mechanism, combined with the abrupt decay of the gmrh horizontal amplitudes outside of the epicentral area, result in a small distance range (which varies with focal depth) in which the mean vertical-component amplitude exceeds the mean gmrh horizontal amplitude.

Figures 8 and 9 extend the comparisons made in Figure 7 to different frequency bands and compare the two rock velocity models using a point-source simulation. Figure 8 shows results for the strike-slip focal mechanism, and Figure 9 shows results for the reverse-faulting mechanism. Figures 8 and 9 show that the general behavior of maximum acceleration amplitude for vertical and gmrh horizontal components described above for the 4–8 Hz passband persists for the 1–2 and 16–32 Hz passbands. Figures 8 and 9 indicate very little difference between the results using the rock-1 and rock-2 models at distances less than approximately 60 km. Differences become appreciable at larger distances, particularly for the vertical component. This is due to



8 Figure 5. Acceleration waveforms for the finite-fault simulation (M 6.0, strike-slip, hypocenter depth 12.25 km) rock-1 velocity model, along a profile trending 22° from the strike direction. (a) Strike-normal horizontal component. (b) Strike-normal horizontal component multiplied by the hypocenter distance r . (c) Vertical component. (d) Vertical component multiplied by the hypocenter distance r . Arrows indicate S_mS reflection from the Moho. Note the very rapid attenuation of the direct S wave on the vertical component, compared to the strike-normal component. At distances exceeding 60 km, the vertical-component maximum amplitude is associated with the Moho reflection.

post-critical reflections from the mid-crustal velocity discontinuity present in the rock-2 model. The vertical component does not show a consistent decrease of amplitude with distance in the 60–120 km range.

Figure 10 plots estimates of the slope of the logarithm of maximum amplitude versus the logarithm of r for the three velocity models and four different focal depths in the six different filter passbands. These estimates were derived from linear regression of the logarithms of acceleration amplitude on hypocenter distance in the range $1.5h$ to 60 km, where h is focal depth. This hypocenter distance range represents the approximately linear section of the log acceleration versus log hypocenter distance plots for the vertical and horizontal components in Figures 8 and 9.

The mean value and standard deviation of all the estimates for the slope of the gmran horizontal component shown in Figure 10 is -1.49 ± 0.31 . It appears that focal depth is not a significant variable in regard to $G(r)$ in the

distance range from $1.5h$ to 60 km for the gmran horizontal component, and no systematic dependence on frequency is apparent in Figure 10. However, the estimates of slope for the reverse focal mechanism are systematically steeper (more negative) than for the strike-slip mechanism for each of the three velocity models examined and for both vertical and gmran horizontal motion.

The range of values of the slope of log maximum amplitude versus $\log r$ for the vertical component exceeds that for the gmran horizontal component, and the slope is steeper. The mean value and standard deviation of all the estimates of slope for the vertical component shown in Figure 10 is -2.63 ± 0.61 . The larger standard deviation for the vertical component reflects the fact that, unlike the gmran horizontal component, the slope for the vertical depends on the focal depth, becoming more negative with increasing depth. The steepest slopes are for the 22.25-km focal depth simulations using the rock-2 model: in that case the hypocenter is

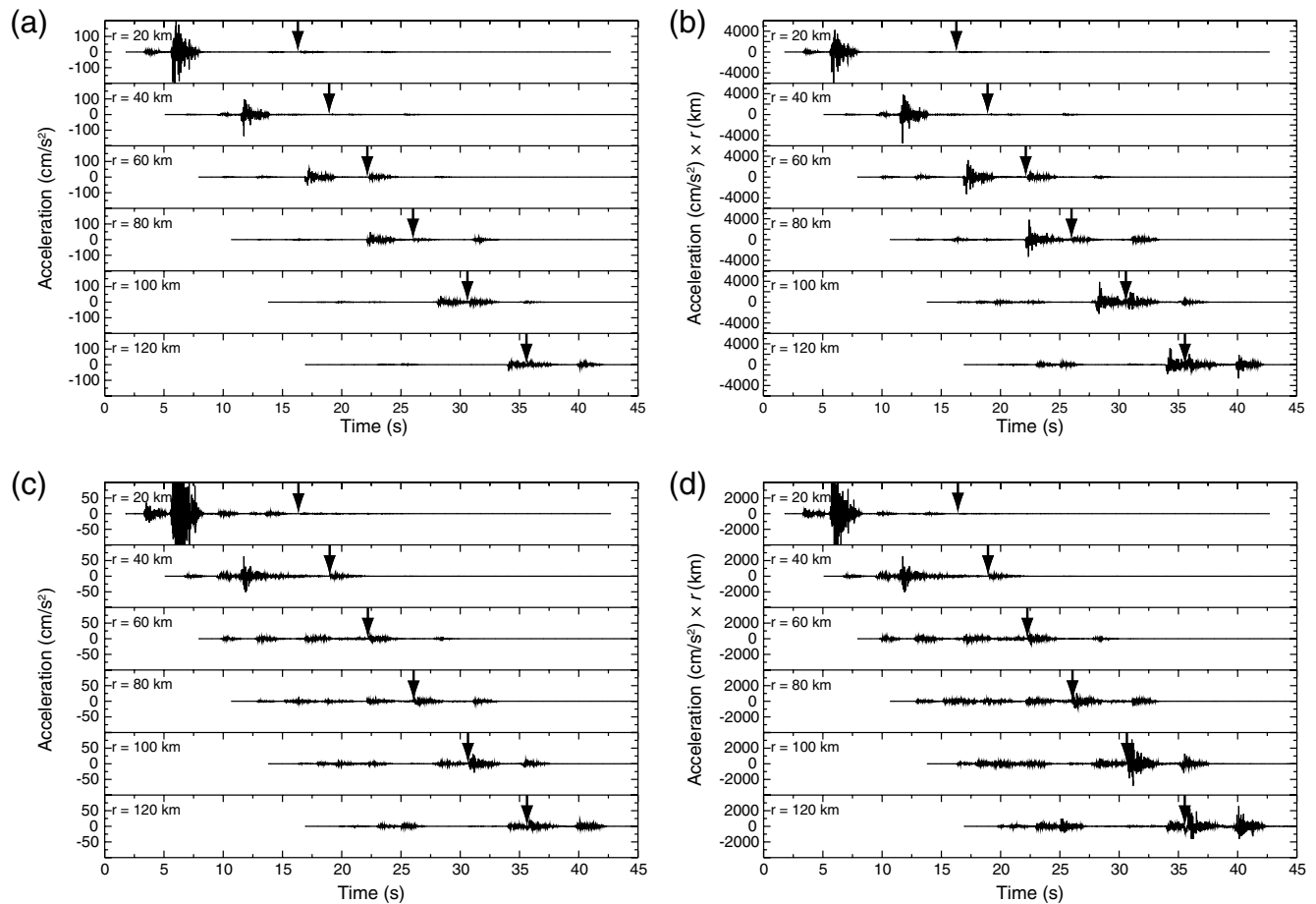


Figure 6. Acceleration waveforms for the finite-fault simulation (M 6.0, reverse fault, hypocenter depth 12.25 km) rock-1 velocity model, along a profile trending 22° from the strike direction. (a) Strike-normal horizontal component. (b) Strike-normal horizontal component multiplied by the hypocenter distance r . (c) Vertical component. (d) Vertical component multiplied by the hypocenter distance r . Arrows indicate SmS reflection from the Moho. Note the very rapid attenuation of the direct S wave on the vertical component, compared to the strike-normal component. At distances exceeding 60 km, the vertical-component maximum amplitude is associated with the Moho reflection.

beneath the mid-crustal velocity discontinuity at 19 km (Fig. 1), a situation that appears to strongly affect the vertical component $G(r)$ function.

Figures 8 and 9 show contrasting, systematic behavior of the vertical and horizontal components that is largely independent of distance, frequency, and focal depth. The horizontal-component (gmran) amplitudes of the reverse-faulting mechanism are smaller than the amplitudes of the strike-slip mechanism beyond a few kilometers from the epicenter of the point-source. In contrast, the vertical-component amplitudes are larger for the reverse-faulting mechanism compared to the strike-slip mechanism. This effect tends to equate the mean amplitude of the vertical and gmran horizontal components for the reverse-fault simulations. In Figure 11, we plot the ratio of the mean amplitude for the reverse focal mechanism to that for the strike-slip focal mechanism, as a function of hypocenter distance, in 2-km-wide distance bins (rock-1 and sediment velocity models). The vertical component is larger for the reverse focal mechanism compared to the strike-slip focal mechanism over most of the hypocenter

distance range, whereas the geometric mean of the randomly oriented horizontal components (gmran) is systematically smaller for the reverse mechanism. This is the case regardless of focal depth, frequency band, or velocity model and is therefore due to the source radiation pattern.

The theoretical modeling predicts that vertical-component amplitudes randomly selected without regard to source–receiver azimuth should, on average, be significantly smaller than the geometric mean amplitude of the horizontal components for strike-slip focal mechanisms at distances slightly outside the epicentral area to approximately 100 km in eastern North America. Testing this prediction with eastern North American data is problematic because of sparse data in the distance range of interest here.

The small-distance data set for reverse-fault earthquakes in eastern North America is larger than for strike-slip events because the majority of well-recorded shocks have occurred in southeastern Canada where reverse faulting dominates (Data and Resources section). As in the case of the strike-slip fault, our modeling of a reverse fault predicts faster

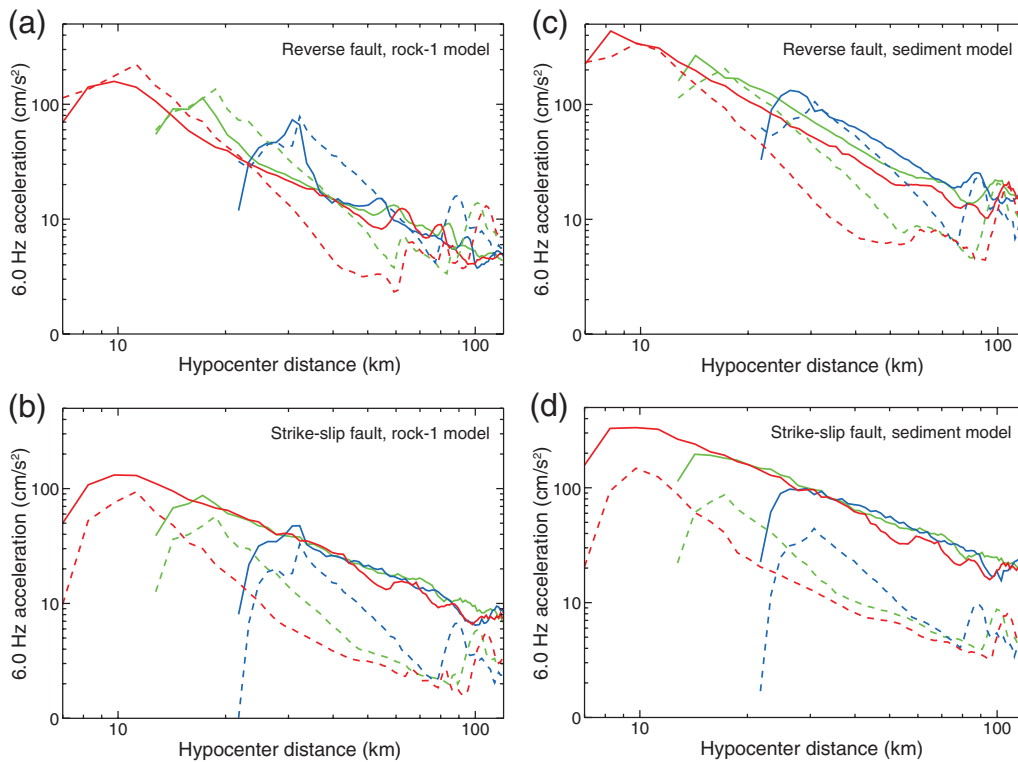


Figure 7. (a,b) Arithmetic mean values of maximum acceleration for the 4–8 Hz frequency band in the 2-km-wide distance bins of the rock-1 velocity model for three different focal depths, as indicated for the reverse and strike-slip mechanisms, respectively. Red, 7-km depth; green, 12-km depth; blue, 22-km depth. The solid lines show values for the geometric mean of the two randomly oriented orthogonal horizontal components (gmran). The dashed lines show values for the vertical component. (c,d) Corresponding results for the sediment velocity model.

geometrical spreading of the vertical component compared to the horizontals, on average, for a large suite of receivers distributed uniformly with respect to azimuth from the source. However, as shown in Figures 7, 8, 9, and 11, the vertical-component amplitudes relative to the gmran horizontal components for the reverse fault are greater than for the strike-slip case. The mean vertical-component amplitudes for the reverse fault are greater than the mean amplitudes of the gmran horizontal components over a significant part of the hypocenter distance range $1.5h$ to 60 km. This holds in particular for the deeper focal depths.

Atkinson (2004), Atkinson (1993) and Siddiqi and Atkinson (2002) have examined the horizontal-to vertical (H/V) amplitude ratios in southeastern Canada and the northeastern United States. They find that H/V is near 1.0 at 1.0 Hz and increases to approximately 1.35 at 10 Hz on rock sites. These observations of H/V near unity are consistent with the results of this study, insofar as the observed data are dominated by reverse-fault earthquakes. A recent example is provided by the 6 March 2005 M 4.6, Riviere du Loup, Quebec, earthquake, which represents the best-recorded mainshock event in eastern North America to date. The preferred focal mechanism reported by Robert Herrmann (Data and Resources section) shows reverse motion (strike 170° , dip 60° , rake 80°) at a depth of 13 km. Figure 12 compares

the amplitude–distance behavior of the vertical and gmran horizontal component 5%-damped PSA response spectra amplitudes for 5 Hz from our M 6.0 finite-fault simulation (reverse mechanism, 12.25 km focal depth) with data observed from the Riviere du Loup event (Boore *et al.*, 2010). Figure 12b shows that a random selection of 25 vertical and gmran horizontal-component values from the simulation bears close resemblance to the observed data from the Riviere du Loup event, if one takes into account the difference in amplitude due to different magnitudes (M 6.0 versus M 4.6). The simulated gmran horizontal-component PSA amplitudes shown by red symbols in Figure 12 generally follow the trend of the Atkinson and Boore (2006) attenuation model, which incorporates geometrical spreading of $r^{-1.3}$ for hypocenter distance less than 70 km, and $r^{+0.2}$ in the 70–140 km range. Observations of geometrical spreading in excess of r^{-1} at small distances have been well-documented by Atkinson and Mereu (1992), Atkinson (2004), and Atkinson and Morrison (2009).

Figure 12b shows that, for sparse data sets, the large amplitude variation due to radiation pattern in the simulated data obscures the systematic differences in vertical and horizontal-component geometrical spreading in the case of a reverse fault. In a combined data set involving both vertical and horizontal-component data, the different geometrical

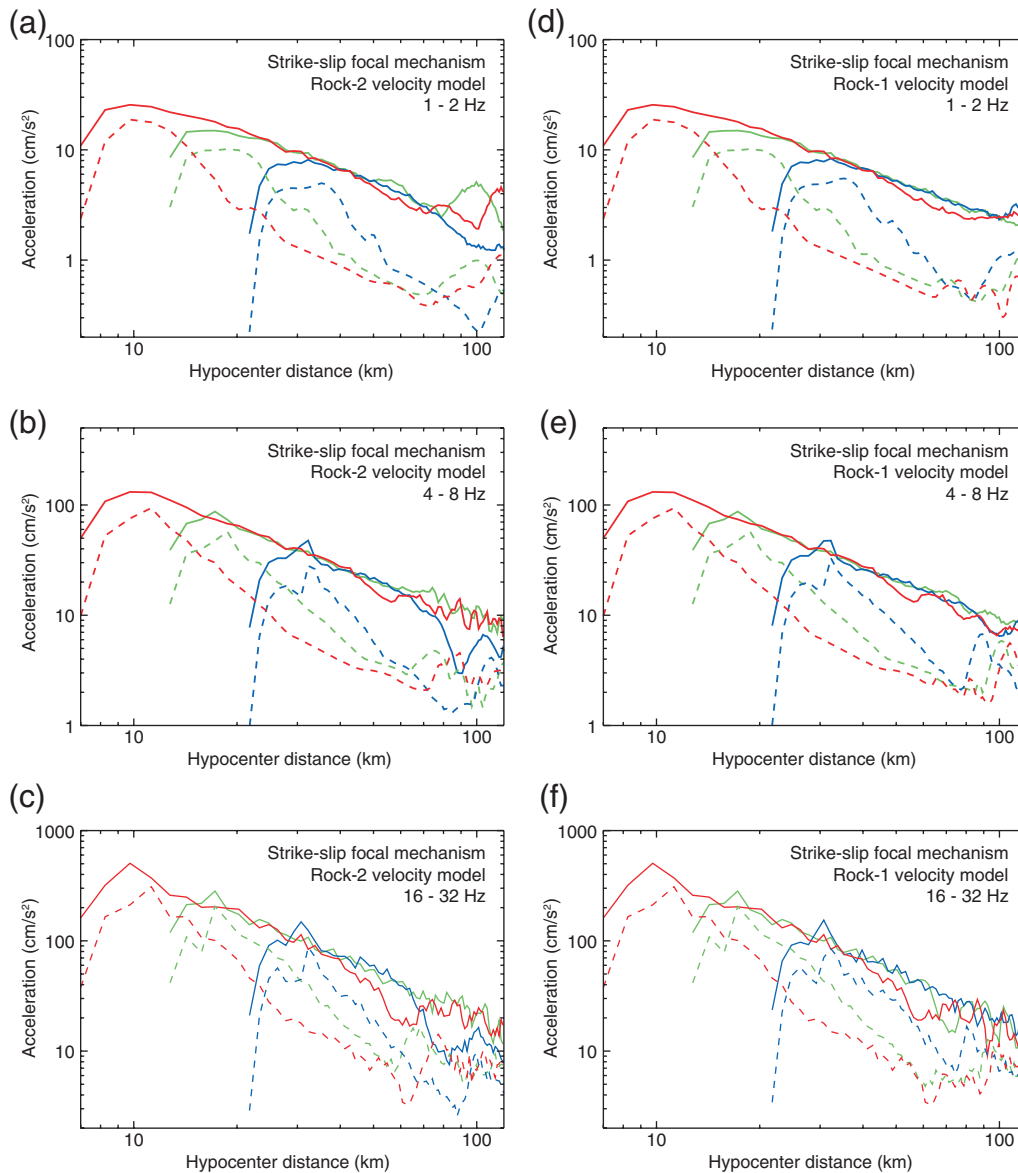


Figure 8. (a,b,c) Arithmetic mean values of maximum acceleration for the 1–2, 4–8, and 16–32 Hz frequency bands, respectively, in 2-km-wide distance bins for the rock-2 velocity model, using three different focal depths and the strike-slip mechanism. Red, 7-km depth; green, 12-km depth; blue, 22-km depth. The solid lines show values for the geometric mean of the two randomly oriented orthogonal horizontal components (gmran). The dashed lines show values for the vertical component. (d,e,f) Corresponding results for the rock-1 velocity model.

spreading of the two components results in scatter in addition to that resulting from the radiation pattern effect for either component considered separately.

Conclusions

Full wave-field simulations using layered, 1D velocity structures show that apparent geometrical spreading of the geometric mean of the maximum acceleration amplitudes of two randomly oriented, orthogonal, horizontal components (gmran), averaged over all azimuths from the source, significantly exceeds the ideal case for body waves in a homogeneous whole space, for hypocentral distances less than

approximately 60 km. These observations are based on the mean values of bandpass-filtered maximum acceleration amplitudes, binned according to hypocenter distance, using a large number of receiver locations surrounding the source.

The behavior of the vertical-component ground acceleration differs from that of the geometric mean of the randomly oriented horizontal component at the frequencies (greater than 0.5 Hz) examined here. At hypocenter distances r in the range $1.5h < r < 60$ km, where h is focal depth, the apparent geometrical spreading of the vertical component $G(r)$ exceeds that of the gmran horizontal, ranging from approximately $r^{-1.5}$ to $r^{-4.0}$. This wide range for the vertical component apparent geometrical spreading at small distances

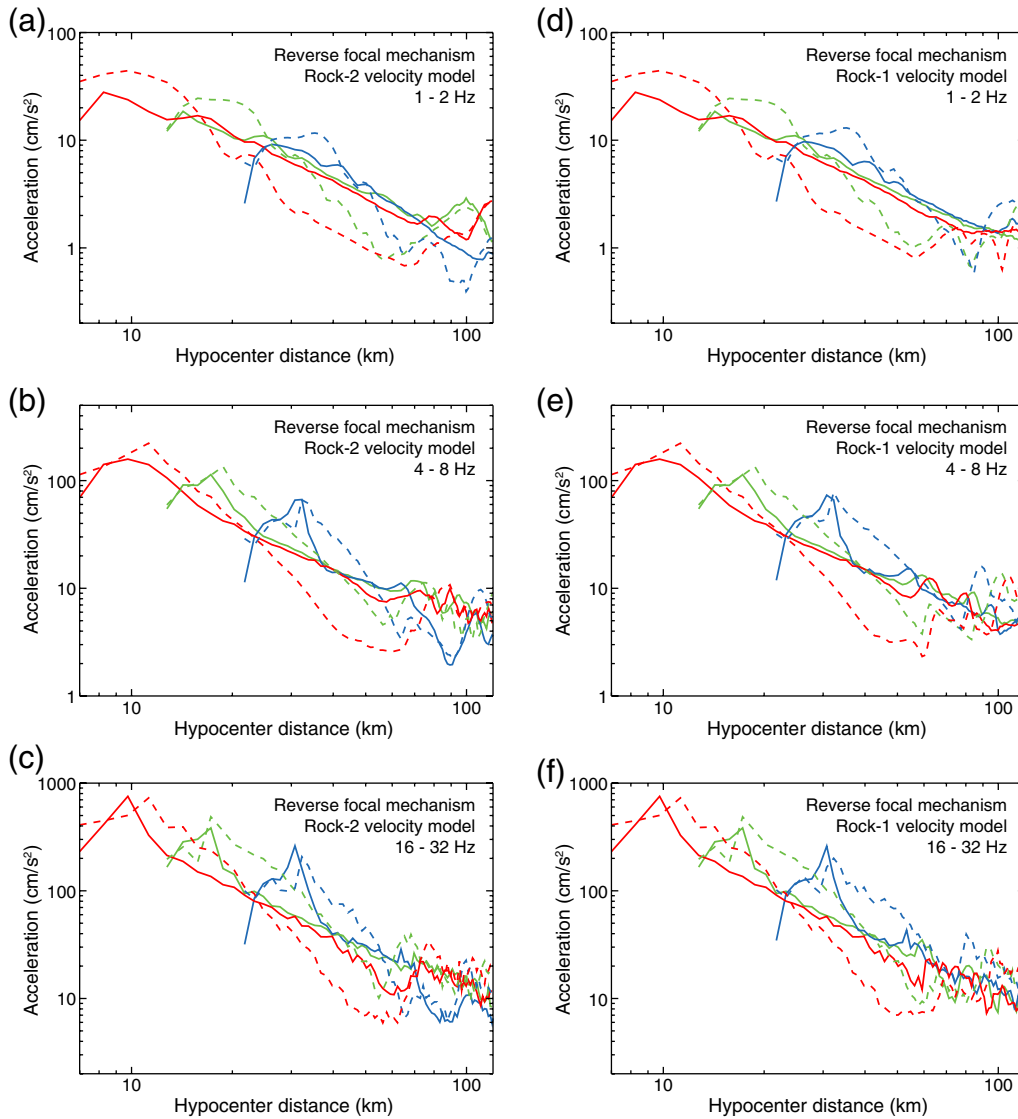


Figure 9. (a,b,c) Arithmetic mean values of maximum acceleration for the 1–2, 4–8, and 16–32 Hz frequency bands, respectively, in 2-km-wide distance bins for the rock-2 velocity model, using three different focal depths and the reverse focal mechanism. Red, 7-km depth; green, 12-km depth; blue, 22-km depth. The solid lines show values for the geometric mean of the two randomly oriented orthogonal horizontal components (gmrn). The dashed lines show values for the vertical component. (d,e,f) Corresponding results for the rock-1 velocity model.

from the epicenter is because of strong dependence on both focal depth and focal mechanism. Apparent geometrical spreading of the vertical component at distances less than 60 km is more rapid for greater focal depths and is systematically more rapid for reverse focal mechanisms (compared to strike-slip) at all depths modeled. Beyond 60 km, the modeled direct *S* wave on the vertical component (averaged over all source–receiver azimuths) is smaller than the vertical-component amplitude of reflections from the mid-crust and Moho, resulting in a zone extending from 60 km to the 120 km limit of the modeling in which maximum amplitudes on the vertical component (averaged over 360° of azimuth from the source) do not decay with distance. This behavior

occurred for all three velocity structures examined here and was independent of frequency.

In contrast to results for the vertical component, the geometric mean of the maximum amplitudes of two randomly oriented, orthogonal horizontal components (gmrn) at distances in the range $1.5h < r < 60$ km for rock sites displays geometrical spreading as approximately $r^{-1.3}$ for strike-slip and $r^{-1.5}$ for reverse-faulting mechanisms, with no significant dependence on focal depth. The apparent geometrical spreading for the deep sediment model is somewhat greater than for the rock models: roughly $r^{-1.5}$ for strike-slip and $r^{-1.9}$ for reverse fault mechanisms. The geometric mean maximum amplitudes of the randomly oriented horizontal

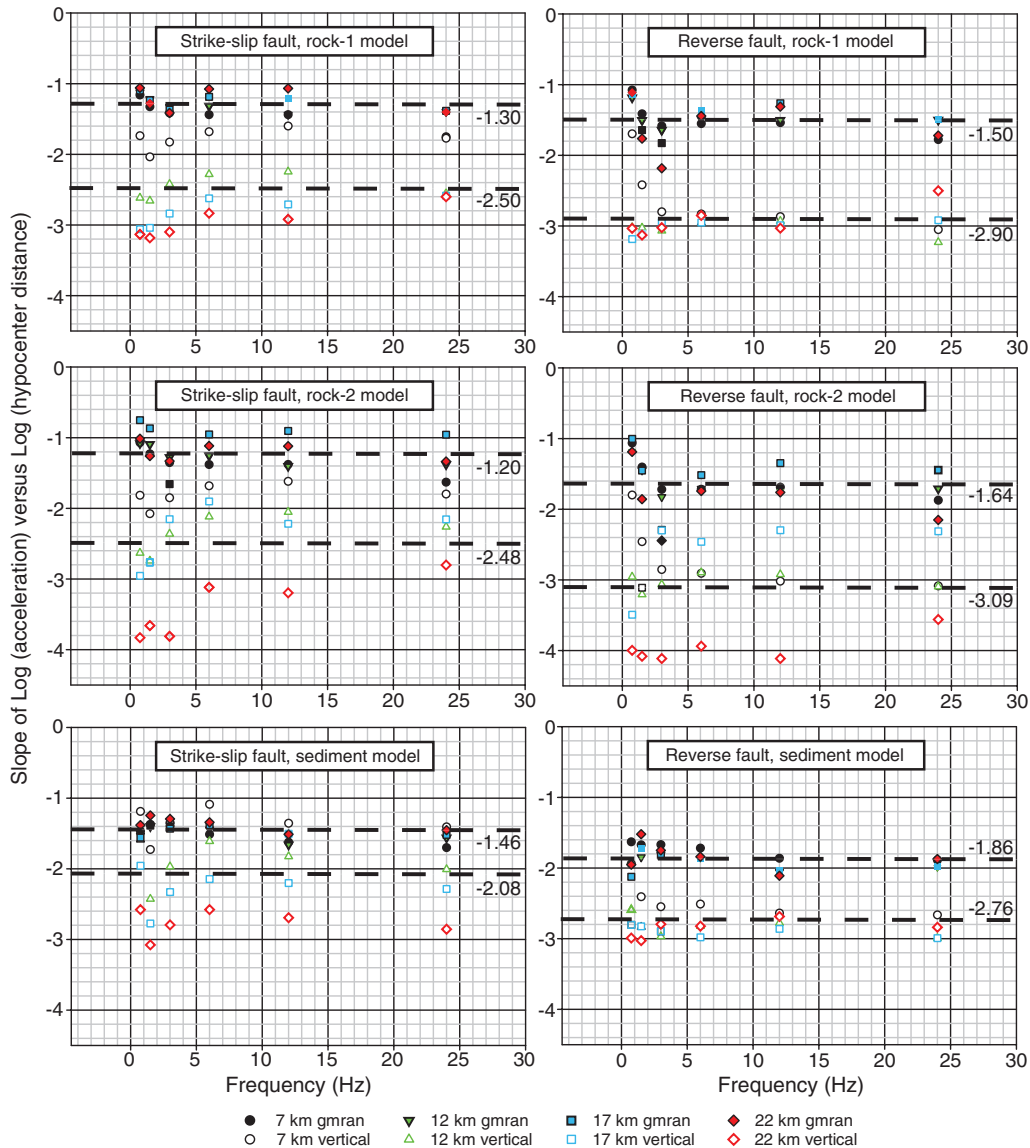


Figure 10. The slope of a linear regression of the logarithm of maximum acceleration on the logarithm of hypocenter distance for each of the rock-1, rock-2, and sediment velocity models, as a function of bandpass filter center frequency, for focal depths of 7.25, 12.25, 17.25, and 22.25 km, and with vertical and geometric mean of randomly oriented horizontal components (gmean). The values plotted are estimates of η for $G(r) = r^{-\eta}$, derived from all simulations in the hypocenter distance ranges 10–60, 18–60, 25–60, and 33–60 km for focal depths 7.25 (circles), 12.25 (triangles), 17.25 (squares), and 22.25 km (diamonds), respectively. Filled symbols are for the gmean horizontal component, open symbols are for the vertical component. Dashed lines with numbers indicate mean estimates, averaged over focal depth and frequency.

components do not exhibit the marked flattening of the vertical component $G(r)$ function in the 60–120 km distance range.

The vertical amplitudes and geometric mean amplitudes of the randomly oriented horizontal components show additional contrasting behavior. Vertical-component amplitudes are from 1 to 2.5 times greater for reverse-fault focal mechanisms, compared to the vertical-component amplitudes from the strike-slip focal mechanisms in the hypocenter distance range from approximately 1.5 times the focal depth to the limit of the modeling at 120 km. The geometric mean amplitudes of the randomly oriented horizontal components in

the same distance range show opposite behavior: the strike-slip mechanisms result, on average, in larger horizontal-component motions, relative to reverse, by factors ranging from 1 to 1.7. These observations are largely independent of focal depth and frequency. The modeling predicts that mean H/V amplitude ratios for strike-slip earthquakes should depend strongly on distance, being larger than unity in the distance range from $1.5h$ to approximately 100 km, an effect that should be easily observable, given appropriate data. In contrast, the reverse-fault modeling suggests that vertical-component amplitudes in the $1.5h$ to 100 km distance range may equal or exceed that of the gmean horizontal components

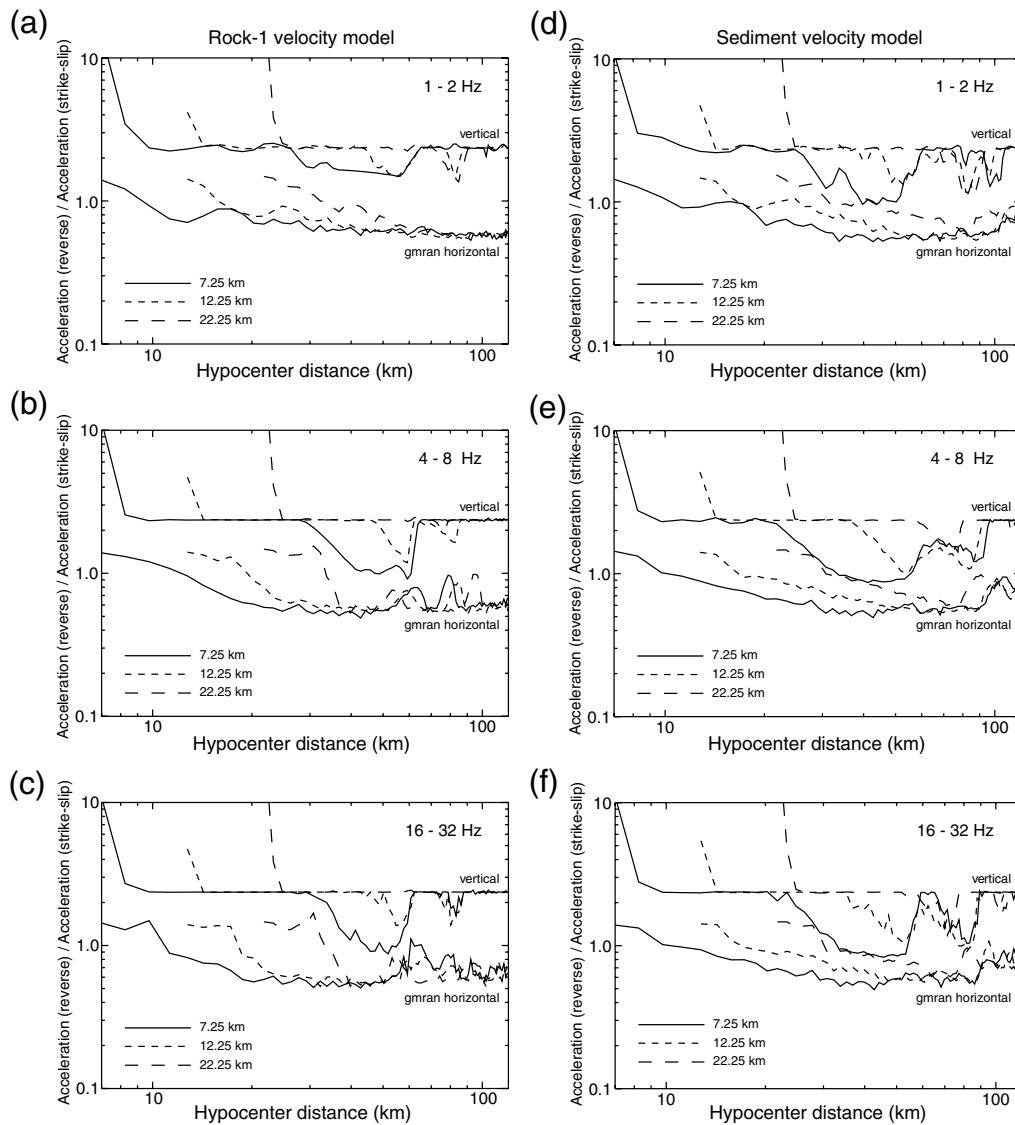


Figure 11. (a,b,c) The ratio of the arithmetic mean acceleration for reverse focal mechanism to that for strike-slip focal mechanism as a function of hypocenter distance in 2-km-wide distance bins for the rock-1 velocity model and passbands 1–2, 4–8, and 16–32 Hz, respectively. (d,e,f) Corresponding results for the sediment velocity model.

when the observations are averaged over a sufficiently wide range of azimuths. Systematic differences in the geometrical spreading of the vertical and horizontal components may be difficult to observe for reverse-fault earthquakes using small data sets because of the scatter due to radiation pattern predicted by the simulations and the effects of site response in real data.

The modeling exercise suggests that ground-motion prediction models should treat the vertical and horizontal-component motions separately in the distance range examined here. Assumptions concerning the ratios of horizontal-to-vertical-component amplitudes that are based on observed behavior of the different components at distances greater than approximately 100 km may not hold at smaller distances, where the modeled amplitude–distance relationship for the vertical component is different from that of the geometric

mean of the two horizontal component amplitudes. The vertical component in this distance range may require prediction models that incorporate dependence on focal depth. The modeling also suggests that much of the aleatory uncertainty in current ground-motion prediction models in the distance range examined here is due to radiation pattern effects.

Data and Resources

Synthetic seismograms were computed using the computer program *hspec96*, version 3.3, developed by Robert Herrmann, Department of Earth and Atmospheric Sciences, St. Louis University, St. Louis, Missouri. That program, user’s guide, and other documentation are contained in *Computer Programs for Seismology*, a software package currently distributed by Herrmann at <http://www.eas.slu.edu/People/>

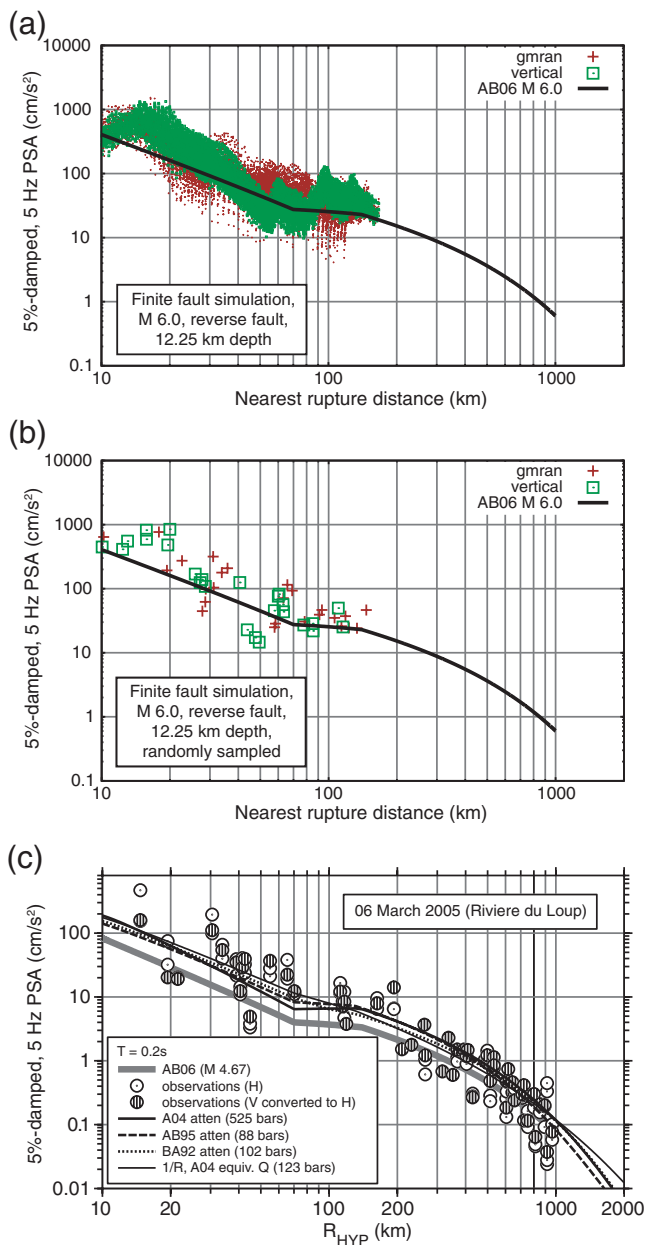


Figure 12. (a) 5%-damped, 5-Hz PSA response spectra values for the finite-fault simulation (M 6.0, focal depth 12.25 km) for the rock-1 velocity model. Red, the geometric mean of randomly oriented horizontal components (gmran); green, vertical component. For reference, the black line shows the Atkinson and Boore (2006) predictions for rock site conditions (M 6.0). (b) A random selection of points from plot (a). (c) Figure reprinted with permission from Boore *et al.* (2010), comparing observations of the 6 March 2005 M 4.67 Riviere du Loup earthquake with several eastern North American ground-motion prediction models. The Atkinson and Boore (2006) model predictions are labeled AB06.

RBHerrmann/CPS330.html (last accessed May 2012). Herrmann has also created an extensive online data base of moment tensor inversions, *North America Moment Tensors*, available at http://www.eas.slu.edu/eqc/eqc_mt/MECH.NA/ (last accessed May 2012).

Acknowledgments

The authors thank the BP High Performance Computing Team for their donation of computing resources, as well as Scott King, Chester Weiss, Ying Zhou, and Advanced Research Computing at Virginia Tech. Reviews and comments from Gail Atkinson, David Boore, and Robert Herrmann improved the study. This research was supported by the U.S. Geological Survey (USGS), Department of the Interior, under USGS award number G09AP00074. The views and conclusions contained in this document are those of the authors and should not be interpreted as necessarily representing the official policies, either expressed or implied, of the U.S. Government.

References

- Atkinson, G. M. (1993). Notes on ground motion parameters for eastern North America: Duration and H/V ratio, *Bull. Seismol. Soc. Am.* **83**, 587–596.
- Atkinson, G. M. (2004). Empirical attenuation of ground-motion spectral amplitudes in southeastern Canada and the northeastern United States, *Bull. Seismol. Soc. Am.* **94**, 1079–1095.
- Atkinson, G. M., and D. M. Boore (2006). Earthquake ground motion prediction equations for eastern North America, *Bull. Seismol. Soc. Am.* **96**, 2181–2205.
- Atkinson, G., and R. Mereu (1992). The shape of ground motion attenuation curves in southeastern Canada, *Bull. Seismol. Soc. Am.* **82**, 2014–2031.
- Atkinson, G. M., and M. Morrison (2009). Observations on regional variability in ground-motion amplitudes for small-to-moderate earthquakes in North America, *Bull. Seismol. Soc. Am.* **99**, 2393–2409.
- Beresnev, I. A., and G. M. Atkinson (1997). Shear-wave velocity survey of seismographic sites in eastern Canada: Calibration of empirical regression method of estimating site response, *Seismol. Res. Lett.* **68**, 981–987.
- Boore, D. M., K. W. Campbell, and G. M. Atkinson (2010). Determination of stress parameters for eight well-recorded earthquakes in eastern North America, *Bull. Seismol. Soc. Am.* **100**, 1632–1645.
- Braile, L. W. (1989). Crustal structure of the continental interior, in *Geophysical Framework of the Continental United States*, L. C. Pakiser and W. D. Mooney (Editors), Memoir 172 Geological Society of America, Boulder, Colorado, 285–315.
- Braile, L. W., W. J. Hinze, R. R. B. von Frese, and G. R. Keller (1989). Seismic properties of the crust and uppermost mantle of the conterminous United States and adjacent Canada, in *Geophysical Framework of the Continental United States*, L. C. Pakiser and W. D. Mooney (Editors), Memoir 172 Geological Society of America, Boulder, Colorado, 655–680.
- Brune, J. N. (1970). Tectonic stress and the spectra of seismic shear waves from earthquakes, *J. Geophys. Res.* **75**, 4997–5009.
- Burger, R. W., P. G. Somerville, J. S. Barker, R. B. Herrmann, and D. V. Helmberger (1987). The effect of crustal structure on strong ground motion attenuation relations in eastern North America, *Bull. Seismol. Soc. Am.* **77**, 420–439.
- Chapman, M. C., and M. J. B. Rogers (1989). Coda Q in the southern Appalachians, *Geophys. Res. Lett.* **16**, 531–534.
- Chapman, M. C., J. N. Beale, and R. D. Catchings (2008). Q for P -waves in the sediments of the Virginia coastal plain, *Bull. Seismol. Soc. Am.* **98**, 2022–2032.
- Chapman, M. C., J. R. Martin, C. G. Olgun, and J. N. Beale (2006). Site-response models for Charleston, South Carolina, and vicinity developed from shallow geotechnical investigations, *Bull. Seismol. Soc. Am.* **96**, 467–489.
- Chulick, G. S., and W. D. Mooney (2002). Seismic structure of the crust and uppermost mantle of North America and adjacent ocean basins: A synthesis, *Bull. Seismol. Soc. Am.* **92**, 2478–2492.
- Frankel, A. (1991). High-frequency spectral falloff of earthquakes, fractal dimension of complex rupture, b -value, and the scaling of strength on faults, *J. Geophys. Res.* **96**, 6291–6302.

- Haskell, N. A. (1953). Dispersion of surface waves in multilayered media, *Bull. Seismol. Soc. Am.* **43**, 17–34.
- Haskell, N. A. (1962). Crustal reflection of plane P and SV waves, *J. Geophys. Res.* **67**, 4751–4767.
- Herrmann, R. B. (1975). A student's guide to the use of P - and S -wave data for focal mechanism determination, *Earthquake Notes* **46**, 29–40.
- Herrmann, R. B., and A. Kijko (1983). Modeling some empirical vertical component Lg relations, *Bull. Seismol. Soc. Am.* **73**, 157–171.
- Kanamori, H., and D. L. Anderson (1975). Theoretical basis for some empirical relations in seismology, *Bull. Seismol. Soc. Am.* **65**, 1073–1095.
- Kennett, B. L. N. (1986). Lg waves and structural boundaries, *Bull. Seismol. Soc. Am.* **76**, 1133–1141.
- Ou, G.-B., and R. B. Herrmann (1990). A statistical model for ground motion produced by earthquakes at local and regional distances, *Bull. Seismol. Soc. Am.* **80**, 1397–1417.
- Siddiqi, J., and G. M. Atkinson (2002). Ground motion amplification at rock sites across Canada, as determined from the horizontal-to-vertical component ratio, *Bull. Seismol. Soc. Am.* **92**, 877–884.
- Silva, W. (1976). Body waves in a layered anelastic solid, *Bull. Seismol. Soc. Am.* **66**, 1539–1554.
- Taylor, S. R. (1989). Geophysical framework of the Appalachians and adjacent Grenville Province, in *Geophysical Framework of the Continental United States*, L. C. Pakiser and W. D. Mooney (Editors), Memoir 172, Geological Society of America, Boulder, Colorado, 317–348.
- Wang, C. Y., and R. B. Herrmann (1980). A numerical study of P -, SV -, and SH -wave generation in a plane layered medium, *Bull. Seismol. Soc. Am.* **70**, 1015–1036.
- Zeng, Y., J. G. Anderson, and G. Yu (1994). A composite source model for computing realistic synthetic strong ground motions, *Geophys. Res. Lett.* **21**, 725–728.

Appendix

Finite-Fault Source Model

The kinematic finite-fault model used here is that developed by Zeng *et al.* (1994) with minor modification. The source is comprised of a set of overlapping circular subfaults. The subfault radii R are randomly distributed according to a power law with fractal dimension $D = 2$ (Frankel, 1991) and minimum and maximum values R_{\min} and R_{\max} . The simulation process begins by specifying a target static moment M_0 and the length L and width W of a rectangular fault-rupture area, with a local 2D Cartesian coordinate system in the fault plane. The subfault center coordinates (x_i, y_i) are drawn from uniform distributions, under the condition that the subfaults lie entirely within the area defined by L and W . The fault width ($W \leq L$) controls the radius of the largest possible subfault, $R_{\max} = W/2$. The total number of subfaults involved in the simulation depends on R_{\min} , R_{\max} , M_0 , and the subfault stress drop $\Delta\sigma^s$. The subfault stress drop is assumed constant.

The number of subfaults with radii greater than R is given by Zeng *et al.* (1994) as

$$N(R) = \frac{p}{D} (R^{-D} - R_{\max}^{-D}), \quad R_{\min} \leq R \leq R_{\max}. \quad (\text{A1})$$

The total number of subfaults involved in the simulation, n , is $N(R_{\min})$ rounded to the nearest integer value. The constant p in equation (A1) is given by (Zeng *et al.*, 1994):

$$p = \frac{7M_0}{16\Delta\sigma^s} \frac{3-D}{(R_{\max}^{3-D} - R_{\min}^{3-D})}. \quad (\text{A2})$$

A random set of subfault radii r_i , $i = 1, 2, \dots, n$, with sizes distributed according to equation (A1), is constructed by evaluation of

$$r_i = \left(\frac{D\gamma_i}{p} + R_{\max}^{-D} \right)^{-\frac{1}{D}}, \quad (\text{A3})$$

(from Zeng *et al.* (1994), their equation 7) where γ_i , $i = 1, 2, \dots, n$ is a set of random, real, numbers with values uniformly distributed from 0 to 1. The static moment of each subfault is (Kanamori and Anderson, 1975)

$$M_0^i = \frac{16}{7} \Delta\sigma^s r_i^3. \quad (\text{A4})$$

The total static moment of the simulation is given by

$$M_0^s = \sum_{i=1}^n M_0^i. \quad (\text{A5})$$

Zeng *et al.* (1994) equate M_0^s and M_0 by adjusting $\Delta\sigma^s$ as necessary. Here, multiple realizations of the set of random subfault radii are created using fixed, independent values of M_0 and $\Delta\sigma^s$. The simulation uses a set of r_i such that the difference between M_0^s and M_0 is negligible; for example, $|M_0^s - M_0| < 0.05M_0$.

The hypocenter (point of rupture initiation) is specified at $x = x_0$, $y = y_0$. A constant rupture velocity, v , is also specified. The moment rate function for the i 'th subfault is assumed to have the same form as the Brune (1970) far-field displacement pulse, that is, 10
11

$$\dot{M}_i(t) = \omega_c^2 (t - \tau_i) M_0^i \exp[-\omega_c^i (t - \tau_i)] H(t - \tau_i), \quad (\text{A6})$$

$$\omega_c^i = \frac{2.34\beta}{r_i}. \quad (\text{A7})$$

In equation (A6), H is the Heaviside function, and $\tau_i = v^{-1} \sqrt{(x_i - x_0)^2 + (y_i - y_0)^2}$ is the delay time associated with travel of the rupture front from the hypocenter to the center of the subfault. In equations (A6) and (A7), ω_c is the subfault corner frequency and β is the shear-wave velocity.

Full wave-field Green's functions are not computed for each subfault because of the large number of subfaults. The rectangular rupture area LW is divided into a grid. The moment rate functions for all circular subfaults with centers inside a particular grid element are summed to produce a moment-rate function for a given grid-element. Let x_j^g and y_j^g , $j = 1, 2, \dots, m$ be the coordinates of the centers of m grid elements of width d . The moment rate for the j 'th grid element is given by 12

$$\dot{M}_j^s(t) = \sum_{i=1}^n C_{ij} \dot{M}_i(t), \quad (\text{A8})$$

where

$$C_{ij} = 1 \quad \text{if } x_j^s - \frac{d}{2} < x_i < x_j^s + \frac{d}{2} \quad \text{and} \\ \text{if } y_j^s - \frac{d}{2} < y_i < y_j^s + \frac{d}{2}, \quad (\text{A9}) \\ C_{ij} = 0 \quad \text{otherwise.}$$

The summation indicated by equation (A8) is performed in the frequency domain. The Fourier transform of equation (A8) is

$$S_j(\omega) = \sum_{i=1}^n C_{ij} \frac{M_o^i}{(1 - \hat{i} \frac{\omega}{\omega_c^i})^2}, \quad (\text{A10})$$

where $\hat{i} = \sqrt{-1}$. The $S_j(\omega)$ are the Fourier transforms of the source time functions (moment rate) for each of the $j = 1, 2, \dots, m$ fault grid elements.

Scaling of Fault Dimensions and High-Frequency Amplitudes

The simulation procedure requires *a priori* knowledge of the scaling of fault-rupture area LW with moment M_o . The above formulation ensures that the static moment of the simulation M_o^s and, therefore, the source spectrum amplitude at frequencies less than the corner frequency (which will lie in the range ν/L to $2\nu/L$ Hz) match the target closely. The source spectrum amplitude at higher frequency depends on the subfault stress drop $\Delta\sigma^s$, which cannot be chosen arbitrarily. As will be shown below, the average spectral amplitude of multiple realizations of the simulation model are not sensitive to R_{\min} , if $R_{\min} \ll R_{\max}$. In what follows, $R_{\min} = R_{\max}/20 = W/40$.

The Brune (1970) model for a circular fault was used as the *a priori* source model to define the fault dimensions L and W and subfault stress drop $\Delta\sigma^s$. From equation (A4), we assume a rupture area

$$A_c = \pi \left(\frac{7M_o}{16\Delta\sigma} \right)^{2/3}, \quad (\text{A11})$$

and assume

$$W = L = \sqrt{A_c} \quad \text{if } A_c < 400 \text{ km}^2, \quad W = 20 \text{ km}, \\ L = A_c/20 \quad \text{if } A_c \geq 400 \text{ km}^2. \quad (\text{A12})$$

13 With $\Delta\sigma = 10$ MPa, the simulated rupture area is a square for $M_o < 5.82 \times 10^{19}$ N·m, or moment magnitude M_w less than 7.14. The assumed maximum width of fault rupture represents the approximate maximum thickness of the seismo-

genic crust in eastern North America, based on earthquake focal depth determinations. The subfault stressdrop $\Delta\sigma^s$ is constrained such that the simulation source spectrum at high frequencies is also consistent with the Brune (1970) model. The Fourier amplitude spectrum of the second derivative of the moment-rate function corresponding to the Brune (1970) model at high frequency (i.e., frequencies much greater than the corner frequency ω_c) is

$$\omega_c^2 M_o = \frac{\pi(2.34\beta)^2}{A_c}. \quad (\text{A13})$$

The corresponding Fourier amplitudes of the simulation source-time function are given by the high-frequency values (e.g., $\omega > 4\pi\nu/L$) of

$$\bar{S}(\omega) = \omega^2 \left| \sum_{j=1}^m S_j(\omega) \right|. \quad (\text{A14})$$

The value of $\Delta\sigma^s$ is determined such that the mean of the high-frequency amplitudes of the simulation (from equation A14) equals the corresponding high-frequency value of the Brune model (equation A13). In practice, this is easily achieved by interpolating results generated from a few simulations using different values of $\Delta\sigma^s$. The proper value of $\Delta\sigma^s$ is always less than the Brune static stress drop $\Delta\sigma$ because the total area of the subfaults is greater than A_c .

Figure A1 illustrates the points discussed above. It shows the target moment and moment rate functions (M_w 6.0, $\Delta\sigma = 10$ MPa) and those of a simulation using $L = W = 6.49$ km, $\Delta\sigma^s = 3.5$ MPa, and $R_{\min} = W/40$. Also shown are the target source amplitude spectrum and three simulation spectra. Two spectra use $\Delta\sigma^s = 3.5$ MPa to match the high-frequency part of the target spectrum. One of those spectra was created using $R_{\min} = W/40$, the other with $R_{\min} = W/80$, to illustrate the effect of changing R_{\min} . The third spectrum uses $\Delta\sigma^s = 0.5$ MPa, $R_{\min} = W/40$. Note that the average values of the two spectra with $\Delta\sigma^s = 3.5$ MPa appears unaffected by the different values of R_{\min} . The (random) differences that are apparent are due to the fact that the random sequences defining the positions and sizes of the subfaults are different; also, the number of subfaults involved in the simulation with $R_{\min} = W/40$ is approximately 1000, whereas approximately 3500 subfaults were used in the case of $R_{\min} = W/80$. The simulation with $\Delta\sigma^s = 0.5$ MPa falls well below the target spectrum at high frequency.

Table A1 lists all the values of the physical parameters used to develop the finite-fault simulations discussed in the text.

Green's Functions and Ground Displacement

The wavenumber integration computer program `hspec96`, version 3.3 (Data and Resources section) was used

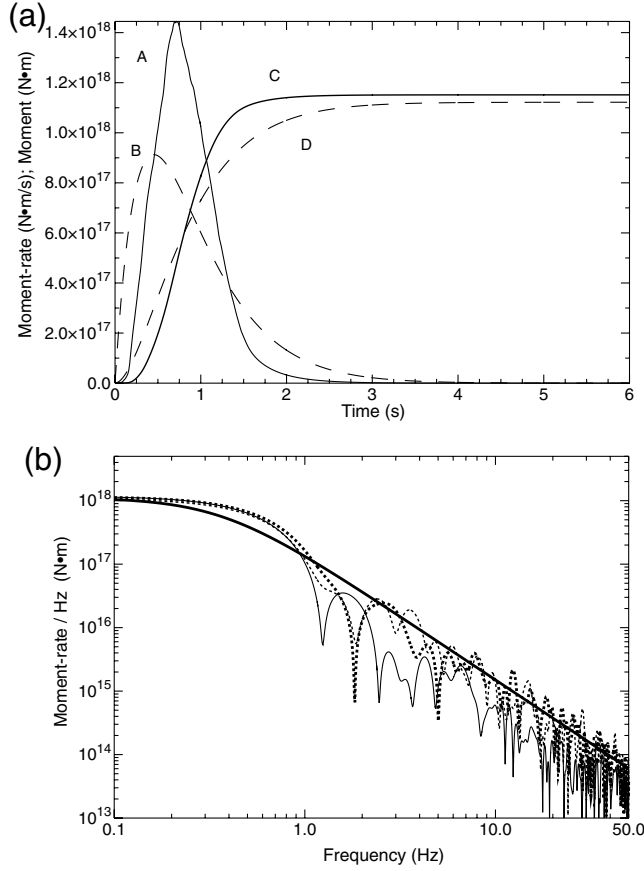


Figure A1. (a) A, simulation source–time function (moment rate) $\dot{S}(t)$; B, moment rate of target (M_w 6, $\Delta\sigma = 10$ MPa, Brune model); C, simulation moment versus time (e.g., $\int_0^t \dot{S}(\tau) d\tau$); D, target moment versus time. (b) Thick solid line, target source amplitude spectrum; thick dashed line, simulation amplitude spectrum with $\Delta\sigma^s = 3.5$ MPa, rupture width 6.49 km, $R_{\min} = W/40$; thin dashed line, simulation with $\Delta\sigma^s = 3.5$ MPa, $R_{\min} = W/80$; thin solid line, simulation with $\Delta\sigma^s = 0.5$ MPa, $R_{\min} = W/40$ (thin solid line).

14 to develop full-wave-field Green’s functions. The Green’s functions include all direct and scattered body waves and surface waves for a horizontally layered Earth model. Anelastic attenuation is incorporated. The wave field includes near-field and far-field components. The Green’s functions are combined with the fault grid-element source functions to

Table A1

Parameters Defining the Finite Fault Simulation

Seismic Moment, M_0^s	1.122×10^{18} N·m
Fault Length, L	6.49 km
Fault Width, W	6.49 km
Static stress drop, $\Delta\sigma$	10 MPa
Subfault stress drop, $\Delta\sigma^s$	3.5 MPa
Maximum subfault radius, R_{\max}	3.245 km
Fault grid element width, d	0.25 km
Fault-rupture velocity, ν	2.8 km/s
Shear wave velocity at hypocenter	3.5 km/s

produce displacements at a specific receiver location on the free surface. Let $u_j^z(\omega)$, $u_j^r(\omega)$, and $u_j^t(\omega)$ represent the vertical, radial, and tangential ground displacements at the receiver due to the j ’th fault grid-element. Following Appendix B-1 of *Computer Programs for Seismology* (Data and Resources section), Wang and Herrmann (1980), and Herrmann (1975), the displacements are given by

$$u_j^z(\omega) = S_j(\omega) \{ zss_j [(f_1 n_1 - f_2 n_2) \cos 2\phi_j + (f_1 n_2 + f_2 n_1) \sin 2\phi_j + zds_j [(f_1 n_3 + f_3 n_1) \cos \phi_j + (f_2 n_3 - f_3 n_2) \sin \phi_j] + zdd_j [f_3 n_3] \} \quad (\text{A15})$$

$$u_j^r(\omega) = S_j(\omega) \{ rss_j [(f_1 n_1 - f_2 n_2) \cos 2\phi_j + (f_1 n_2 + f_2 n_1) \sin 2\phi_j + rds_j [(f_1 n_3 + f_3 n_1) \cos \phi_j + (f_2 n_3 + f_3 n_2) \sin \phi_j] + rdd_j [f_3 n_3] \} \quad (\text{A16})$$

$$u_j^t(\omega) = S_j(\omega) \{ tss_j [(f_1 n_1 - f_2 n_2) \sin 2\phi_j - (f_1 n_2 + f_2 n_1) \cos 2\phi_j + tds_j [(f_1 n_3 + f_3 n_1) \sin \phi_j - (f_2 n_3 + f_3 n_2) \cos \phi_j] \} \quad (\text{A17})$$

In equations (A15)–(A17), ϕ_j is the source–receiver azimuth (reckoned clockwise, east of north). The quantities zss_j , zds_j , and zdd_j are the Green’s functions for vertical-component surface displacement due to a slip-rate impulse on a strike-slip, 90° dip-slip, and 45° dip-slip fault, respectively, at the epicentral distance and depth position in the Earth model corresponding to the center of the j ’th fault grid-element. Similarly, rss_j , rds_j , and rdd_j are for the radial component (elemental strike-slip, 90° dip-slip, and 45° dip-slip, respectively). The Green’s functions for the tangential component of surface displacement, tss_j and tds_j correspond to impulse slip-rate on a vertical strike-slip fault and 90° dip-slip fault, respectively. Unit vectors $\vec{f}(f_1, f_2, f_3)$ and $\vec{n}(n_1, n_2, n_3)$ are in the direction of slip and normal to the fault, respectively. They can be expressed in terms of fault strike ϕ_f , fault dip d_f , and rake λ_f (measured counterclockwise in the fault plane from the strike direction) as

$$f_1 = \cos \lambda_f \cos \phi_f + \sin \lambda_f \cos d_f \sin \phi_f, \quad (\text{A18})$$

$$f_2 = \cos \lambda_f \sin \phi_f - \sin \lambda_f \cos d_f \cos \phi_f, \quad (\text{A19})$$

$$f_3 = -\sin \lambda_f \sin d_f, \quad (\text{A20})$$

$$n_1 = -\sin \phi_f \sin d_f, \quad (\text{A21})$$

$$n_2 = \cos \phi_f \sin d_f, \quad (\text{A22})$$

and

$$n_3 = -\cos d_f. \quad (\text{A23})$$

The complete vertical U_z , fault strike-normal horizontal U_n , and fault strike-parallel horizontal U_p components of displacement at the receiver are created by summing over all the grid-elements:

$$U_z(\omega) = \sum_{j=1}^m u_j^z(\omega), \quad (\text{A24})$$

$$U_n(\omega) = \sum_{j=1}^m [u_j^r(\omega) \cos\left(\varphi_j - \phi_f - \frac{\pi}{2}\right) + u_j^t(\omega) \cos(\phi_j - \phi_f)], \quad (\text{A25})$$

and

$$U_p(\omega) = \sum_{j=1}^m \left[u_j^r(\omega) \cos(\varphi_j - \varphi_f) + u_j^t(\omega) \cos\left(\phi_j - \phi_f + \frac{\pi}{2}\right) \right] \quad (\text{A26})$$

The summation operations approximate continuous integration over the fault-rupture surface. The error introduced by this approximation is proportional to d , the width of the fault grid element. The consequences of this approximation are explored in Figure A2, which compares the effect of grid element size on the strike-normal horizontal component of velocity and acceleration simulated for a vertical, right-lateral, strike-slip fault (M 6.0, $\Delta\sigma = 10$ MPa). The receiver is located in the plane of the fault, 14 km in the strike direction from the nearest point of subsurface rupture. Figure 4 shows velocity computed using unique Green's functions for each of 1005 subfaults within a 6.49×6.49 km² rupture area. The Green's functions include the direct P and S wave and all the scattered waves with the same ray parameters as the direct arrivals (Haskell, 1953, 1962; Silva, 1976). Also shown is the result of applying a reduced number of single ray parameter Green's functions by gridding the fault into elements with width $d = 0.25$ km and $d = 1.0$ km. Figure A2 also shows the full wave-field synthetics (solid lines) for the two grid-element sizes. We observe good agreement between the velocity waveforms computed using the smaller grid-element and the ungridded waveform and relatively poor agreement using the larger element size. The velocity model used in this experiment includes a complex crustal structure (36 layers) between the ground surface and the top of the fault at 4 km depth. However, the chief difference between the single ray parameter and full wave-field velocity waveforms is the existence of the near-field component in the

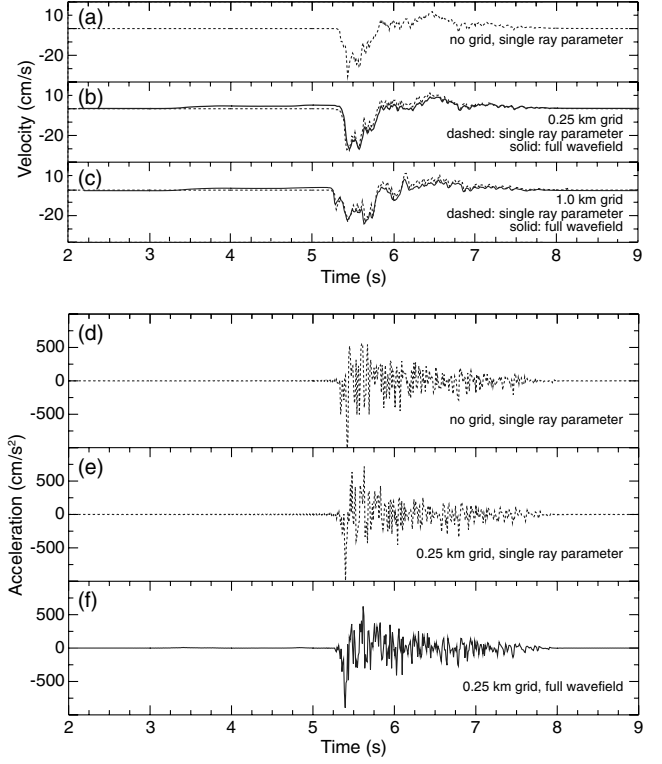


Figure A2. (a) Fault strike-normal horizontal component of velocity for an M 6.0, $\Delta\sigma = 10$ MPa, right-lateral strike-slip fault simulation created with unique single ray parameter Green's functions for each subfault. The receiver lies in the plane of the fault and is 14 km from the nearest point of subsurface rupture. (b) Simulation using 0.25-km-wide grid elements. The dashed line shows results from a single ray parameter simulation; the solid line shows the full wave-field simulation. (c) As in (b), but using 1.0-km-wide fault grid elements. (d) Fault strike-normal horizontal component of acceleration, created with unique single ray parameter Green's functions for each subfault. (e) Acceleration, single ray parameter simulation using 0.25-km-wide fault grid elements. (f) Acceleration, full wave-field simulation.

full wave field, apparent between the P wave arrival time (at approximately 3.2 seconds) and the S wave arrival. Note that the far-field P wave is absent (radiation pattern is null) in this example. The convention here is for the positive fault strike-normal horizontal component to be in the horizontal direction of fault dip: this is to the right for an observer looking in the strike direction. The fault strike-parallel horizontal component is positive in the strike direction. Figure A2 shows the acceleration waveforms as well. The gridded acceleration waveforms exhibit the amplitude and general characteristics of the ungridded version. The differences are attributable to effects at frequencies greater than 2.0 Hz. A comparison of the Fourier amplitude spectra in Figure A3 shows that for a 0.25-km grid element width, the gridded and ungridded spectra match almost exactly at frequencies less than 2 Hz. A similar calculation for a site located normal the fault plane at the point of rupture initiation at the center of the fault shows good agreement between gridded and nongridded simulations to approximately 10 Hz (Fig. A3). The effect

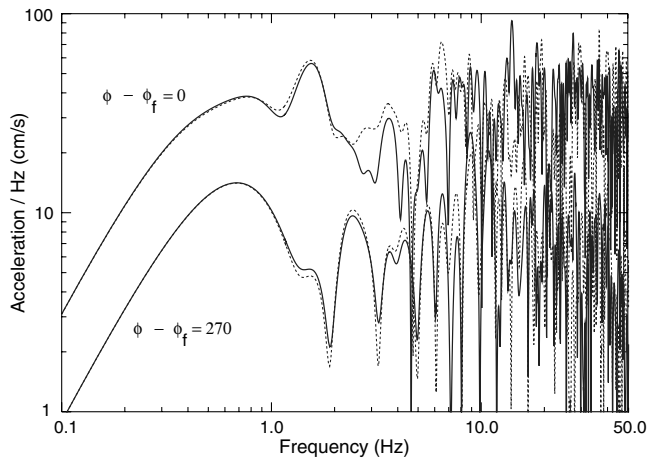


Figure A3. The upper solid line shows the fault strike-normal acceleration spectra for an M 6.0, $\Delta\sigma = 10$ MPa, right-lateral strike-slip fault simulation created using a unique single ray parameter Green's function for each subfault. The receiver lies in the plane of the fault and is 14 km from the nearest point of subsurface rupture. The upper dashed line indicates the acceleration spectrum derived by using 0.25-km-wide grid elements. The lower solid line shows the acceleration spectrum for a receiver azimuth normal to the fault, at a distance of 20.4 km from the nearest point of rupture, created using a unique single ray parameter Green's function for each subfault. The lower dashed line shows the acceleration spectrum derived using 0.25-km-wide fault grid-elements. The lower spectra are multiplied by a factor of 0.33 for illustration.

of gridding in the application of the Green's functions is very complicated: it introduces a complex spectrum modulation at the higher frequencies. However, it does not result in sys-

tematic bias of the high-frequency source spectrum amplitudes. Rather, the effect resembles that which would occur if the ungridded high-frequency source spectrum were multiplied by a white noise spectrum with unit mean amplitude.

Point-Source Simulations

Wave propagation effects are similar for point-source models and the finite-fault models, at distances large in comparison to fault-rupture dimensions. The Fourier transform of the source-time function for the point-source simulation $S^p(\omega)$ is simply the sum of the individual functions for each fault grid element, given by equation (A10).

$$S^p(\omega) = \sum_{j=1}^m S_j(\omega). \quad (\text{A27})$$

This source function is applied at a single point in the center of the fault rupture and the number of Green's functions implied by equations (A15)–(A17) are reduced from m (the number of fault grid elements) to 1, for a given receiver location.

Department of Geosciences
 Virginia Polytechnic Institute and State University
 4044 Derring Hall
 Blacksburg, Virginia 24061 U.S.A.
 mcc@vt.edu

Manuscript received 16 March 2011

Queries

1. AU: Please check the email address of the corresponding author.
2. AU: Both “full-wave-field simulations” (hyphen after “full”) and “full wave-field simulations” are used in your article. Please review ALL uses of the term, and use the following as a guide to determine which definition of the phrase was intended in EACH case:
 - full-wave-field simulations—refers to simulation of a full wave field
 - full wave-field simulations—refers to full simulation of wave fields
3. AU: Please verify whether EarthScope transportable array should be changed to EarthScope Transportable Array (as a proper name).
4. AU: Please check all uses of “high-frequency” and “high frequency” (hyphenated and nonhyphenated). Both versions were used for what appeared to be the same type of descriptions.
5. AU: BSSA does not allow quotation marks in this context. Please provide alternative wording if just deleting the quotation marks presents a problem.
6. AU: Should this be “2-km-wide”? Otherwise it means 2 separate bins, 1 km wide each – I have changed all instances to “2-km-wide” where the compound acts as an adjective.
7. AU: Please verify whether this is the definition you intended for H/V.
8. AU: (1) The captions for Figures 5 and 6 are exactly alike with the exception for Figure 5 caption using “strike-slip” and Figure 6 using “reverse fault.” Please verify whether this is as you intended. (2) Please especially check the edit that adds parentheses to the first sentence to be sure that your intended meaning has not been changed.
9. AU: Please verify that the letter “o” as subscript is correct here. (Moment magnitude uses zero, but I am unsure for static moment.)
10. AU: Please verify that the letter “o” as subscript is correct here.
11. AU: Is the prime required in ith? For the ordinal, BSSA uses i-th (hyphen), if that is what you intended here. This will be changed throughout the appendix if you indicate the hyphen is correct
12. AU: As with ith queried previously, should jth be written as j-th (replace the prime with a hyphen)? This will be changed throughout the appendix if you indicate the hyphen is correct
13. AU: Please verify whether this is intended to be moment magnitude. If so, then we will need to change the letter “o” to a non-italic subscript zero.
14. AU: As with “full-wave-field simulations” vs. “full wave-field simulations, please clarify which is correct for Green’s functions: (1) full wave-field Green’s functions (meaning full Green’s functions) or (2) full-wave-field Green’s functions (meaning full wave fields). ALSO, may this form be used to standardize the term throughout the entire article?
15. AU: Please verify the figure number. Figure 4 shows acceleration, not velocity.
16. AU: You have been using “single ray parameter” (no hyphen) in the captions for Figs. A2 and A3 when the phrase is used as an adjective, as well as “single-ray parameter Green’s function” in the caption for Fig. A3. I have tentatively deleted the hyphen here and in the second use of the phrase in the caption for Fig. A3 for consistency, but please indicate whether your article should be standardized to use (1) single ray-parameter Green's functions or (2) single ray parameter Green's functions.
17. AU: Please review the use of “normal” in the phrase “for a site located normal the fault plane,” and provide alternative wording if needed.